ISSN 1063-7834, Physics of the Solid State, 2020, Vol. 62, No. 2, pp. 368–377. © Pleiades Publishing, Ltd., 2020.
Russian Text © The Author(s), 2020, published in Fizika Tverdogo Tela, 2020, Vol. 62, No. 2, pp. 316–325.

GRAPHENES

Effect of Magnetic Co–CoO Particles on the Carrier Transport in Monolayer Graphene

J. A. Fedotova[a], A. A. Kharchanka[a, *], A. K. Fedotov[a], M. V. Chichkov[b], M. D. Malinkovich[b], A. O. Konakov[c], S. A. Vorobyova[c], J. V. Kasiuk[a], U. E. Gumiennik[a], M. Kula[d], M. Mitura-Nowak[e], A. A. Maximenko[e], J. Przewoźnik[f], and Cz. Kapusta[f]

[a] *Institute for Nuclear Problems, Belarusian State University, Minsk, Belarus*
[b] *National University of Science and Technology "MISiS," Moscow, Russia*
[c] *Research Institute for Physical Chemical Problems, Belarusian State University, Minsk, Belarus*
[d] *Franciszek Górski Institute of Plant Physiology, Polish Academy of Sciences, Krakow, Poland*
[e] *Institute of Nuclear Physics Polish Academy of Sciences, Krakow, Poland*
[f] *Department of Solid State Physics, Faculty of Physics and Applied Computer Science, AGH University of Science and Technology, Krakow, Poland*
**e-mail: XaaTM@mail.ru*

Received September 17, 2019; revised September 17, 2019; accepted September 24, 2019

Abstract—Electrodeposition of cobalt on monolayer graphene synthesized by chemical vapor deposition produces Co–CoO/graphene composite structures, which is accompanied by increases in the electrical resistance and magnetoresistance. We show that the observed magnetoresistance effect is caused by two competing contributions: negative (NMR) and positive (PMR) magnetoresistance. In weak magnetic fields, the NMR is described by quantum localization correction to the Drude model of conductivity in graphene. The enhancement of PMR observed in strong magnetic fields is related to the Lorentz mechanism in Co–CoO particles.

Keywords: graphene, cobalt, cobalt oxide, carrier transport

DOI: 10.1134/S1063783420020134

1. INTRODUCTION

Fabrication and studying of magnetic and magnetoresistive graphene-based composite structures is a highly relevant problem, because it opens new perspectives for their use in magnetic tunneling transitions, spin valves and filters, magnetoresistive memory devices, and other spintronic elements [1–3]. These kinds of structures can be successfully fabricated by depositing particles or layers of various ferromagnetic materials (e.g., Co and Ni) onto graphene [2, 4]. We note that investigation of specific characteristic of deposition and agglomeration of metallic particles deposited on graphene is one of the issues related to its prospective use in electronic devices since requires to overcome the difficulty of making low-resistance ohmic contacts to the graphene surface.

To date, there have been relatively few experimental and theoretical studies on the magnetic and galvanomagnetic properties of structures composed of a ferromagnetic metal and graphene such as Co nanoparticles or isolated Co islands deposited on graphene synthesized by chemical vapor deposition (CVD) [1, 4, 5]. Using X-ray photoelectron spectroscopy and magnetic measurements, these studies showed that the deposited cobalt particles were markedly oxidized at the surface and often represented a structure of the Co core–CoO shell type. Nevertheless, electrochemical deposition produces good (barrier-free) ohmic electrical contacts, as was confirmed in [5]. Among different mechanisms of low-temperature carrier transport and magnetotransport in pure graphene, the interference mechanism is typically used within the theory of quantum corrections to the Drude model of conductivity subject to the condition of weak localization [6–8]. Another conductivity mechanism frequently used in this respect is the variable-range hopping model within the Mott model [9], Efros–Shklovsky [10] model (the case of zero magnetic field), and Mikoshiba [11] and Altshuler–Aronov–Khmelnitsky [6] models for carrier transport in a nonzero magnetic field. For composite metal–graphene structures with a metal shunting, we cannot eliminate the presence of the extraordinary magnetoresistance effect observed in high transversal magnetic fields [12].

With electrochemical deposition, nucleation of metal nanoparticles was shown to take place specifically in regions with morphological alterations, including those caused by residual copper fragments that formed after transferring a graphene sample onto a Si/SiO_2 substrate [13].

The findings of previous studies thus suggest that the situation at the metal/graphene interface and defectiveness of the initially obtained graphene play a key role in determining the carrier transport and magnetotransport characteristics of composite metal/graphene structures, especially at low temperatures.

The aim of this work is to investigate the interrelation between the electric and magnetic properties of composite structures consisting of a ferromagnetic metal and graphene that are fabricated by electrochemical deposition of cobalt nanoparticles onto monolayer CVD graphene, since this will enable us to identify the effects that cobalt islands have on carrier transport in zero and nonzero external magnetic fields.

2. EXPERIMENTAL TECHNIQUES AND SAMPLE PREPARATION

Graphene was synthesized on copper foil by CVD using a PlanarTech G2 unit. Acetylene was used as a carbon precursor, and hydrogen was fed into the reactor alongside acetylene for dilution; the ratio of gaseous components was $C_2H_2 : H_2 = 1 : 4$. The process was carried out at 1040°C at a pressure of 6 Torr. Synthesized graphene was transferred using polymethylmethacrylate (PMMA). For this, a 4% solution of the polymer in anisole was applied on a copper foil/graphene sample inside a spin coating system that was operated at a rate of 1500 rpm. The resulting sample was baked in an oven at a temperature of 150°C. Copper foils were subsequently etched in an aqueous ferric chloride solution. The resulting PMMA film was rinsed twice with deionized water and placed on a substrate. The film was dried, while in the spin coater, at a rate of 3000 rpm, then heated at a temperature of 120°C in order to remove folds. The PMMA layer was dissolved away in acetone.

Cobalt nanoparticles were deposited onto graphene from a solution containing 1.25 g/L $CoSO_4 \cdot 6H_2O$ and 0.064 g/L NaCl using a PI-50-1.1 potentiostat coupled to a PR-8 programming unit. Depositions were performed in the pulse reverse mode, a controlled-current technique, at a cathodic current density of 2.5 mA/cm^2 (pulse duration, 5 s) and anodic current density of 1.25 mA/cm^2 (pulse duration, 2 s); the total deposition time was 30 s.

Raman spectroscopy was carried out on a Nicolet Almega XR Raman microscopy system equipped with Omnic 8 software (Thermo Fisher Scientific, USA). The laser excitation wavelength was 532 nm, and the laser power was around 0.1 W. Raman spectra were collected in the range of 400 to 4000 cm^{-1}. The slit width was 2.5 μm, and the working distance was determined by a 100× objective of the microscope. Sixty-four spectral acquisitions were carried out. Samples were placed on the microscope stage and a laser beam was focused at a specimen surface. Each sample was investigated in three different regions.

Scanning electron microscopy (SEM) imaging was performed using a Vega 3 instrument (Tescan) in the secondary electron detection mode, with the accelerating voltage being 30 kV. Atomic force (AFM) and magnetic force (MFM) microscopies were carried out on a XE-120 microscope (Park System Corporation) in the contactless mode. For these investigations, we used a MAGT cantilever with a coated tip (a 40 nm thick CrCo layer) with a radius of curvature <40 nm (AppNano). Before use, the tip was magnetized along its vertical axis in a magnetic field with $B = 0.5$ T. MSM imaging followed the surface topography imaging and was performed at a probe-to-surface distance of 200 nm.

Magnetic measurements were carried out in the temperature range of 2–300 K in the magnetic fields up to 9 T using the vibrating-sample magnetometer option of a Physical Property Measurement System (Quantum Design).

Temperature and magnetic field dependences of electrical resistivity $R(T, B)$ were measured by the four-point probe method in the temperature range of 2 to 300 K and in a transversal magnetic field with magnetic flux density B up to 8 T using a noncryogenic measuring system (Cryogenics Ltd) on the basis of a closed-cycle refrigerator. In studying $\rho(T, B)$ and $R_H(T, B)$ dependences, current through a sample was controlled and measured using a Keithly 6430 apparatus, which enabled us to measure the electrical resistance in the range of 100 μΩ to 10 GΩ with an accuracy of at least 0.1%. The temperature of samples was measured using LakeShore thermal diodes calibrated to an accuracy of 0.0005 K and having a precision of 0.001 K, which enabled us to stabilize and measure the temperature using a LakeShore 331 temperature controller. The accuracy of resistivity measurements and the Hall coefficient was at least 5%, with the main factors contributing to the experimental error being inaccuracies in the measurements of the sample geometrical dimensions, width of probable electrical contacts, and distance between them.

3. RESULTS AND DISCUSSION

The structure of samples of CVD graphene with deposited Co nanoparticles (Co–*Gr*/SiO_2) was investigated using Raman spectroscopy, and the results are shown in Fig. 1.

Overall, the characteristics of our *Gr*/SiO_2 and Co–*Gr*/SiO_2 samples are typical of monolayer graphene, as was confirmed by a number of methods. The number of graphene layers was determined by evaluating the shape and measuring the width of the

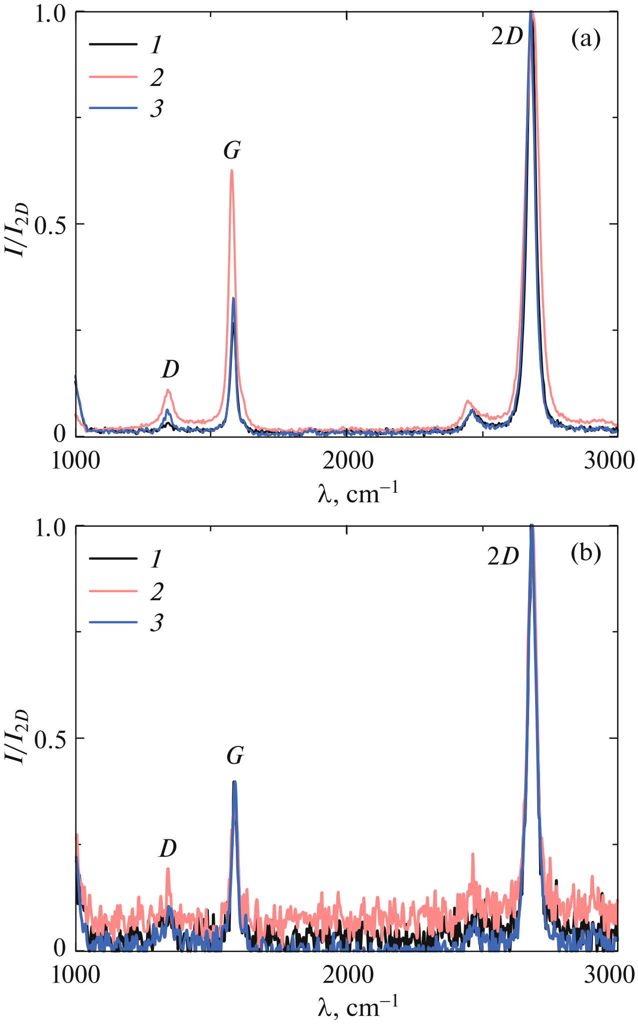

Fig. 1. Raman spectra for (a) *Gr*/SiO$_2$ and (b) Co–*Gr*/SiO$_2$ samples.

2*D* peak [14], as well as by using the intensity ratio between the 2*D* and *G* peaks [15, 16]. The 2*D* band in the Raman spectra of the *Gr*/SiO$_2$ and Co–*Gr*/SiO$_2$ samples represents a Lorentzian with a full width at half-maximum of ≈40 cm^{-1}, which are the features typical of monolayer graphene [14]. On the other hand, the intensity ratio for *Gr*/SiO$_2$ and Co–*Gr*/SiO$_2$ samples is on average $I_{2D}/I_G > 2$, another indicator of monolayer graphene [15, 16]. At the same time, the sample contains regions (Fig. 1a, curve *2*) with characteristics of bilayer graphene: the intensity ratio is $I_{2D}/I_G = 1.595$ (for bilayer graphene, $1 < I_{2D}/I_G < 2$), and the 2*D* peak is broader. The intensity ratio between *D* and *G* peaks (i.e., I_D/I_G) enables us to estimate the amount of defects in a graphene sample. For the *Gr*/SiO$_2$ sample, we have the intensity ratio $I_D/I_G <$ 0.2, a value typical of large-area polycrystalline films with a fairly decent sample quality [17]. The Co–*Gr*/SiO$_2$ sample exhibits a slight increase in the I_D/I_G ratio, but can still be considered as having a fairly decent quality.

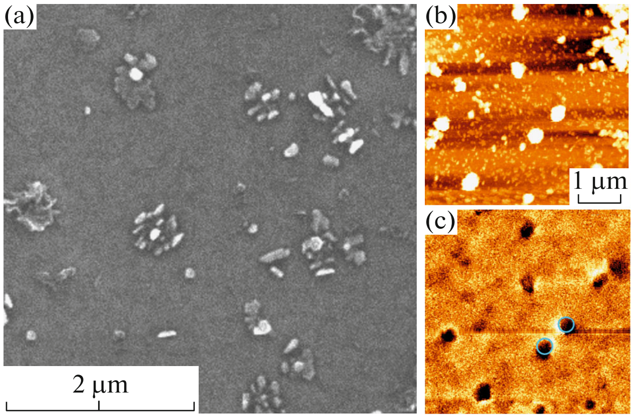

Fig. 2. Morphology of Co–*Gr*/SiO$_2$ sample: (a) SEM, (b) AFM, and (c) MFM images.

Additionally, we estimated the number of graphene layers using the relationship $\omega_G = 1581.6 + 11/(1 + n^{1.6})$, where ω_G is the *G* band position and *n* is the number of graphene layers [18]. The position of *G* band in the spectra of Co–*Gr*/SiO$_2$ sample agrees well with the theory, which additionally corroborates that our samples are monolayer graphene with inclusion of bilayer regions. For the *Gr*/SiO$_2$ sample, however, the *G* band has a lower Raman shift (i.e., 1577 cm^{-1}), which is out of the range predicted by the theory, and this deviation was attributed to changes in the carrier concentration [19]. Deposition of cobalt particles caused the *G* band to return to 1587 cm^{-1} the absolute value for the layer Hall coefficient R_Hd (which is negative) to increase. The latter was measured at room temperature in a magnetic field $B = 1$ T, and the values were 126 and 485 m^4/C for the *Gr*/SiO$_2$ and Co–*Gr*/SiO$_2$ samples, respectively.

A surface topography SEM image of the Co–*Gr*/SiO$_2$ sample is shown in Fig. 2a. The analysis of contrast features in the image showed that the Co deposition produced mainly isolated particles with a size of around 50 nm and agglomerates (size up to 500 nm) consisting of prolate particles. The regions with a bright contrast in the image may correspond to completely or partially oxidized particles, and the latter are likely represent the Co core–CoO shell type structure, as was proven in [5]. The results of SEM agree well with AFM images (Fig. 2b). These AFM images show that the particles and their agglomerates are not spherical, because their size in the image plane exceeds their height by 30–40%. Contrast features seen in MFM images (Fig. 2c) are typical when imaging is performed using a probe magnetized perpendicularly to the sample's plane; these are characteristic of cobalt island nanostructures that have their easy mag-

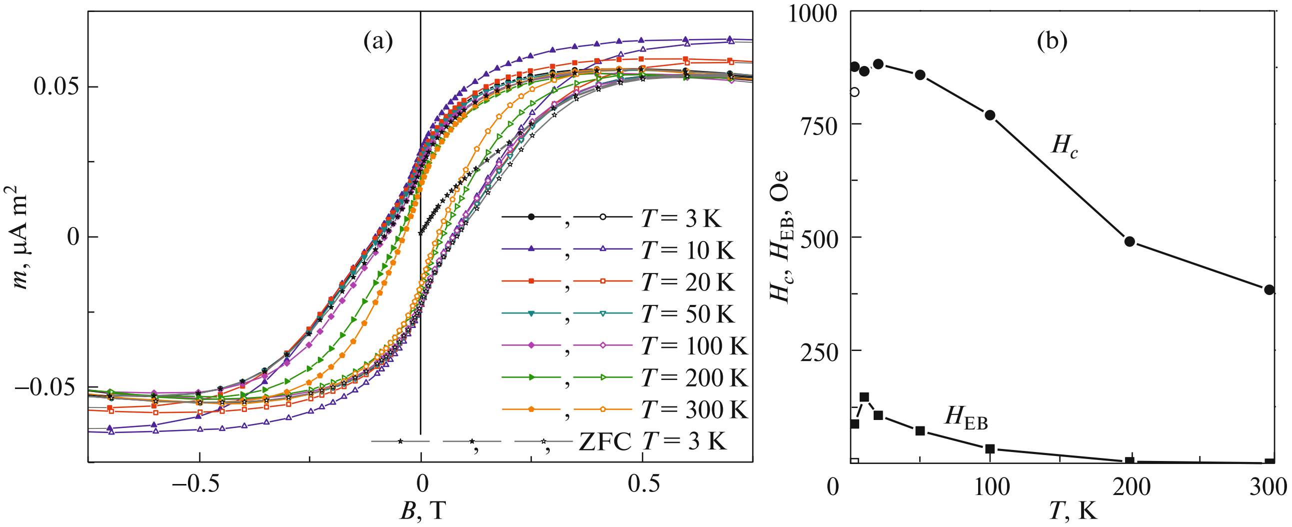

Fig. 3. Co–*Gr*/SiO$_2$ sample: (a) $m(B)$ magnetization curves and (b) temperature dependences of coercive field H_c and exchange bias (magnetic field) H_{EB}.

netization axis in the sample's plane [20, 21]. In this instance, large agglomerations (size, 400–500 nm) of deposited particles are seen as regions with bright contrast at one end and dark contrast on the other end, which corresponds to a strong interaction between the probe and magnetic poles of nanostructures that have their magnetic moments lying in the sample's plane (i.e., a magnetic dipole response) [22]. Isolated nanoparticles and smaller agglomerates are likely to be magnetically soft, exhibit a weak interaction with the tip, and do not exhibit noticeable magnetic contrast.

The magnetic state of Co–*Gr*/SiO$_2$ samples was additionally investigated by magnetometry. Magnetization curves for these samples were recorded in the temperature range of 3–300 K and are shown in Fig. 3a. The magnetization curves $m(B)$ recorded at room temperature (T = 300 K) are nearly symmetric (relative to B = 0 T). They are characterized by coercivity $B_C \approx 38$ mT and saturations at relatively small B (around 0.4 T), suggesting that the remaining unoxidized cobalt makes a sufficient contribution to the magnetization of Co–*Gr*/SiO$_2$ samples. As the temperature T is reduced below 100 K, the $m(B)$ curves become asymmetric relative to the zero B field. This suggests the presence of exchange bias that reaches field strengths H_{EB} up to 146 Oe at T = 10 K (Fig. 3b). The observed exchange bias and sufficiently large coercivity H_C (up to 880 Oe at 20 K) are most likely due to exchange interaction at the Co core/CoO shell interface. Similar results were obtained for Co particles electrodeposited onto twisted graphene [5]. Considering that H_{EB} is inversely proportional to the size of ferromagnetic particles [23], the relatively small values of H_{EB}, with respect to for example H_{EB} = 6.5 kOe for Co–CoO particles at T = 10 K [24], are indicative of quite a large size of Co cores in the deposited Co–CoO particles.

In addition, the $m(T)$ curves recorded at $T \leq 100$ K show a inflection at fields around B = 0.15 T. This shape of the curves may be suggestive of the nonuniform size of the deposited particles due to their complex core–shell type structure. In this instance, nonoxidized cobalt cores undergo remagnetization at smaller B fields, while the inflection on $m(T)$ curves corresponds to the beginning of remagnetization in regions close to the oxide shell which exhibit a harder magnetic behavior due to the effect of spin pinning at the core–shell interface. The fact that the inflection on the curves occurs below the Néel temperature (T_N) for CoO [25] supports this hypothesis.

The temperature dependences of sheet resistance $R_\square(T)$ for *Gr*/SiO$_2$ (curve *1*) and Co–*Gr*/SiO$_2$ (curve *2*) samples are shown in Fig. 4 in normalized (Fig. 4a) and semilogarithmic (Fig. 4b) coordinates. The linearity of current–voltage curves shown in the inset in Fig. 4b is indicative of the ohmic behavior of electrical contacts. The shape of curves *1* and *2* suggests that $R_\square$ increased after electrodeposition of particles and that the shape of $R_\square(T)$ dependence is associated with a semiconducting behavior at temperatures below 150–200 K. Moreover, the data of Fig. 4 show an abrupt drop in the resistance in curve *2* (see the inset to Fig. 4a) at temperatures above 260 K, which may be related to the phase transition in the CoO shell (or isolated CoO particles) from the antiferromagnetic to paramagnetic state at a temperature above the Néel temperature [25]. We note that the observed increase in the electrical resistance of Co–*Gr*/SiO$_2$ sample, compared to its *Gr*/SiO$_2$ counterpart, may be due to the presence of CoO. We also note that, as the tem-

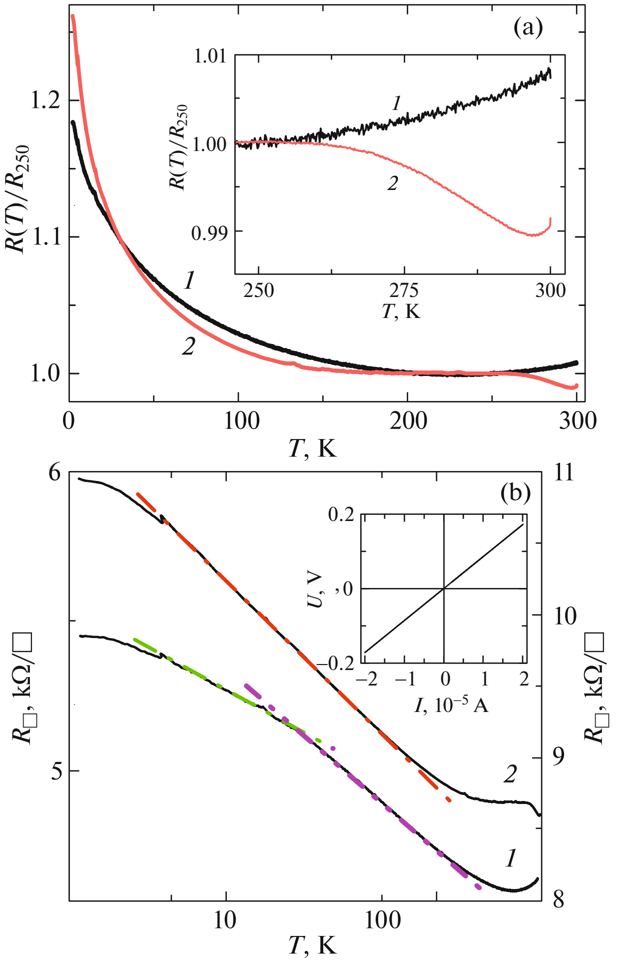

Fig. 4. Temperature dependences of sheet resistance $R_\square(T)$ in (a) normalized and (b) semilog coordinates for (*1*) Gr/SiO_2 and (*2*) Co–Gr/SiO_2 samples. Inset to Fig. 4a: a magnified view of $R_\square(T)$ dependence in the range of 240–300 K. Inset to Fig. 4b: current–voltage curve for the Co–Gr/SiO_2 sample recorded at room temperature.

perature is raised (above 225 K for Gr/SiO_2 and 290 K for Co–Gr/SiO_2), the sign of temperature coefficient of electrical resistance flips from positive to negative, which points to a metal-like behavior of these samples at elevated temperatures.

The important feature of samples under study is that the $R_\square(T)$ dependences shown in Fig. 4b (i.e., in the $R_\square(T)$–$\log T$ semilog coordinates) tend to exhibit a linear behavior (corresponding curve regions are marked with colored lines) and the tendency to saturation, as the temperature is reduced. The observation of linear regions on the curves presented in the $R_\square(T)$–$\log T$ coordinates is usually ascribed to the presence of quantum corrections to the Drude model subject to the condition of weak localization [6–8, 26]. The estimative calculations provided below suggest that incoherence of the phase of electrons that are related to the mentioned linear contribution (behavior) is due to their elastic scattering on phonons [27]. The likelihood of this scenario is also indicated by a fairly broad linear behavior range for the $R_\square(T)$–$\log T$ dependences (i.e., from 5 to 100 K). Such a behavior is not uncommon for graphene [28], which places it in stark contrast to metals and semiconductors, for which weak quantum localization effects are observed at temperatures no more than 10–15 K [29]. This fact can be linked to specific features of the phonon spectrum of carbon nanolayers, and in particular to that the Debye temperature θ_D for graphene is much higher than that for any other quasi-two-dimensional systems on the basis of metals or semiconductors. For graphene, θ_D reaches 1200–2300 K [30]. As a result, even at temperatures around 200 K, the energy and density of excited phonons are low enough to result in quasi-elastic scattering of electrons on phonons [27].

The saturation behavior of $R_\square(T)$ curves (Fig. 4b) may be due to a drop in the conductivity of graphene layer to the minimum for disordered metallic systems (the so-called minimum metallic conductivity $\sigma_{\min}$), as the temperature tends to the absolute zero [27]. An alternative explanation of the observed saturation is that the free path becomes comparable to the grain size in graphene, as the temperature is lowered [31].

Knowing that disorder may break the weak localization conditions and lead to a strong localization which prepares ground for hopping conductivity in graphene, we tested this hypothesis by fitting the $R_\square(T)$ curves with the known formula

$$R(T) \approx R_0^D \exp\left[\left(\frac{T_0^D}{T}\right)^{\alpha}\right]. \tag{1}$$

In this formula, the model parameters α, R_0^D, and T_0^D depend on the mechanism of hopping conductivity, the dimensionality (1, 2, or 3) of samples under study, and the energy-dependence of density of localized states involved in hopping. In the Mott model of variable-range hopping conductivity, parameter α can take values of 0.25 or 0.33 for the 3D and 2D variants, respectively, while the Shkolovskii–Efros model gives 0.5 and 0.33 for α for the 3D and 2D variants, respectively [9, 10, 32]. We note that, in the conventional band model of conductivity, parameter $\alpha = 1$.

To identify possible involvement of one of the mentioned models of variable-range hopping conductivity, relationships $R_\square(T)$ are conventionally plotted in so-called Mott coordinates, i.e., $\ln(R_\square(T))$–$(1/T)^{\alpha}$, in which low-temperatures regions of Mott curves are linearized for one of the indicated values of α in the exponent in Eq. (1). The slope of these linear sections in the Mott coordinates (i.e., $\ln(R_\square(T))$–$(1/T)^{\alpha}$) can be used to estimate parameters R_0^D and T_0^D, which determine the probability of hopping and the wave

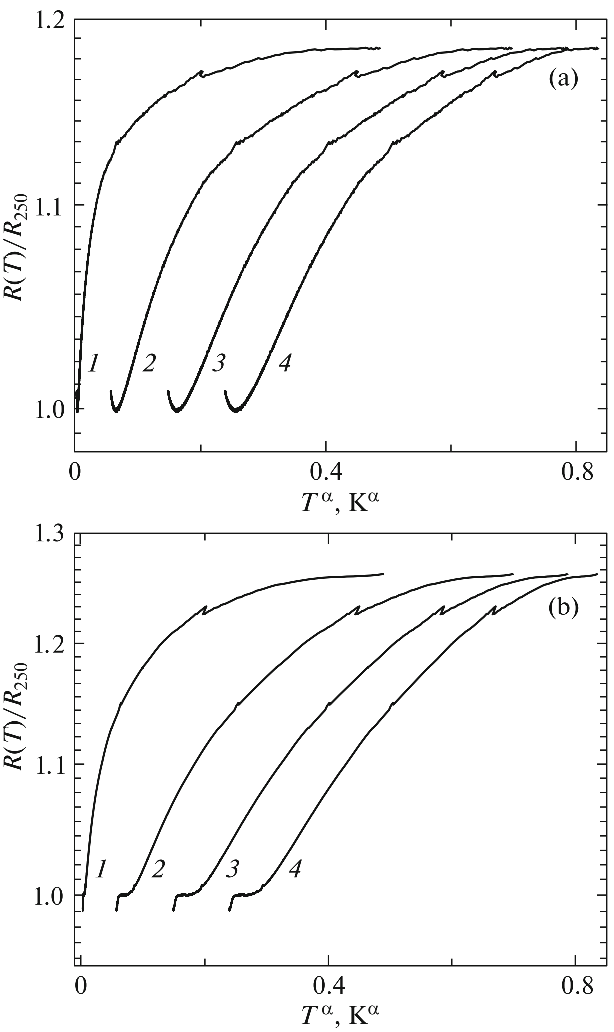

Fig. 5. Temperature dependences $R_\square(T)$ in the Mott coordinates $(\ln(R_\square(T))–(1/T)^\alpha)$ for (a) *Gr*/SiO$_2$ and (b) Co–*Gr*/SiO$_2$ samples at different values for exponent α in Eq. (1): (*1*) 1, (*2*) 1/2, (*3*) 1/3, and (*4*) 1/4.

function localization radius in the corresponding models. The $R_\square(T)$ dependences in Fig. 5 show us that our experimental data in low-temperature ranges are consistent with none of the mentioned models, since no linear sections of these curves are observed. This means that, for our graphene samples, the shape of $R_\square(T)$ curves at lower temperatures is mainly determined by the theory of quantum corrections to the Drude model of conductivity.

To reaffirm the validity of this statement, we analyze the field-dependences of sheet resistance $R_\square(B)$ and relative magnetoresistance $MR(B) = [R_\square(B, T) - R_\square(0, T)]/R_\square(0, T)$ for the *Gr*/SiO$_2$ and Co–*Gr*/SiO$_2$ samples under study, which are shown in Figs. 6 and 7, respectively. As Fig. 6 shows, the initial graphene (i.e., *Gr*/SiO$_2$) is characterized by two contributions to the magnetoresistance effect: the negative (NMR) and the positive (PMR) one. For the *Gr*/SiO$_2$ sample, the NMR is observed in only weak fields (up to 0.4–0.8 T), but here it covers almost the entire temperature range under study (up to 250 K, as the PMR starts to take place from this temperature upward). These two effects compete at low temperatures (2–175 K), so that the PMR starts dominating in magnetic fields with flux density more than 1 T. That being so, the *MR*(*B*) dependences in the range of very low temperatures (i.e., 2–5 K) in fields higher than 4–5 T are quite linear, whereas the *MR*(*B*) curves follow a quadratic dependence in fields <4 T, which may be suggestive of the Lorentz force acting upon electrons. For the Co–*Gr*/SiO$_2$ sample, the $R_\square(B)$ and *MR*(*B*) dependences tend to a plateau at low temperatures (2–10 K) and in magnetic fields higher than 6 T (curves *1*–*3* in Fig. 7).

By comparing Figs. 6 to 7, we can see that electrodeposition of cobalt nanoparticles on graphene leads to narrowing both the temperature and magnetic field ranges for NMR—below 75 K and 0.5 T, respectively—and enhancement of the contribution of PMR to the total magnetoresistance. In contrast to the *Gr*/SiO$_2$ sample, for which the *MR* grew by only 23%, a marked increase of 80% was registered for the Co–*Gr*/SiO$_2$ sample in a field of 8 T (i.e., in the PMR region). The presence of this enhancement may tell us that the effect of Lorentz force on the electrons in CoO cores is implicated in the PMR effect in samples under discussion, which, in turn, means that the shell is not continuous and has pinholes that result in a direct electrical contact between graphene and Co cores.

The effects that magnetic field and electrodeposition of oxidized cobalt particles have on the type of magnetoresistance effect (i.e., a switch from NMR to PMR) and can be appreciated from temperature dependences *MR*(*T*) registered at different *B* (Fig. 8). In the low-temperature range, in which the PMR is dominant, *MR*(*T*) for the *Gr*/SiO$_2$ sample initially increases and then tends to saturation (curves *1* and *2* in Fig. 8a). The transition to PMR, occurring as the temperature is raised, causes the *MR* to increase in response to raising the temperature or increasing the applied magnetic field (curves *3*–*6* in Fig. 8a), reaching saturation at room temperatures as well. At the same time, we can see that (Fig. 8b), for samples with deposited oxidized cobalt particles, *MR* grows at all temperatures and the *MR*(*T*) dependences exhibit a marked change in their shape. Although these curves continue to exhibit a saturation behavior at small *B*, in stronger fields, i.e., $B > 3$ T, they have maxima that tend to shift toward lower temperatures: starting from 220 K at $B = 4$ T to 150 K at $B = 8$ T.

To identify the role that temperature plays in switching the type of magnetoresistance effect from NMR to PMR, in Fig. 9, we show the dependences for $MR_{\min}$

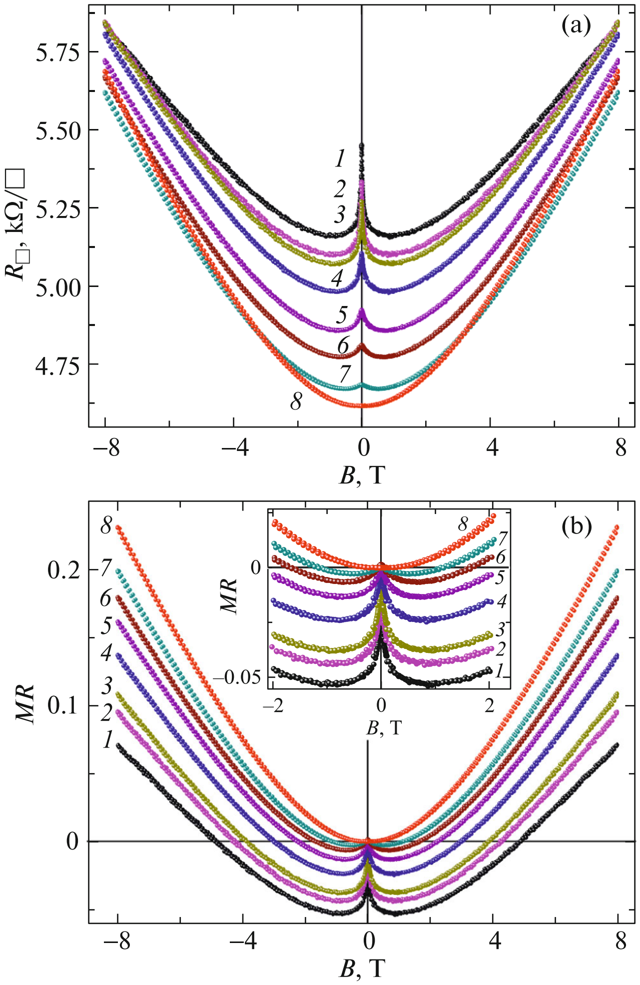

Fig. 6. Dependences of (a) sheet resistance $R_\square(B)$ and (b) relative magnetoresistance $MR = [R_\square(B) - R_\square(0)]/R_\square(0)$ on magnetic flux density B for *Gr*/SiO$_2$ sample at different temperatures covering the range of 2–300 K: (*1*) 2, (*2*) 7, (*3*) 10, (*4*) 25, (*5*) 50, (*6*) 75, (*7*) 125, and (*8*) 275 K. Inset to Fig. 6b: *MR* curves in the range of magnetic flux density of $-2 \le B \le 2$ T.

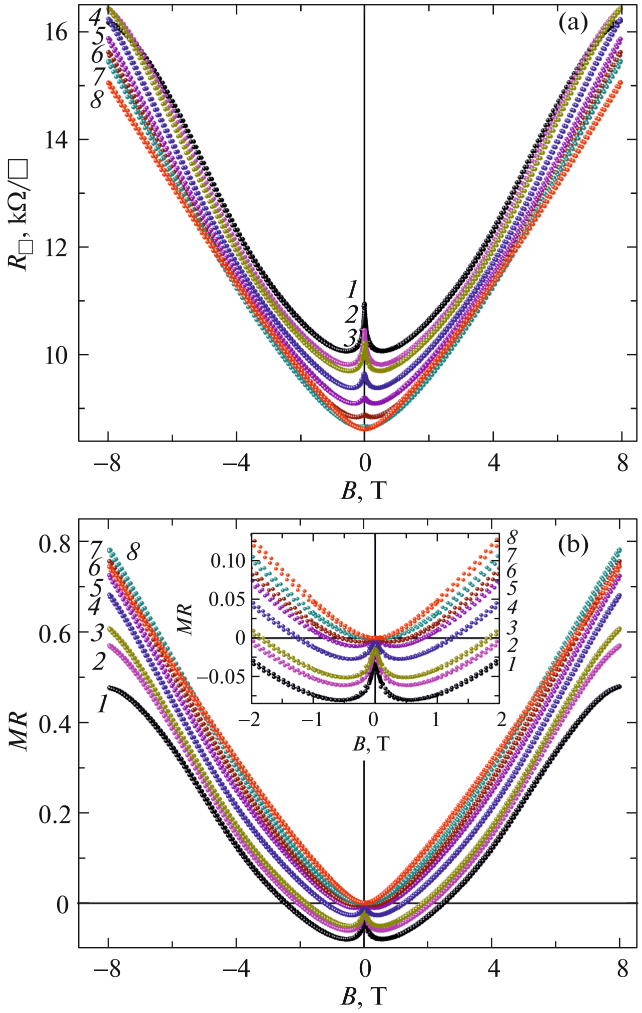

Fig. 7 Dependences of (a) sheet resistance $R_\square(B)$ and (b) relative magnetoresistance $MR = [R_\square(B) - R_\square(0)]/R_\square(0)$ on magnetic flux density B for Co–*Gr*/SiO$_2$ sample at different temperatures covering the range of 2–300 K: (*1*) 2, (*2*) 7, (*3*) 10, (*4*) 25, (*5*) 50, (*6*) 75, (*7*) 125, and (*8*) 275 K. Inset to Fig. 7b: *MR* curves in the range of magnetic flux density of $-2 \le B \le 2$ T.

(curves *1*) and $B_{\min}$ (curves *2*) at the minima of $MR(B)$ dependences shown in Figs. 6 and 7 for the two samples. It can be seen that absolute values of both $MR_{\min}$ and $B_{\min}$ drop rapidly (nearly linearly) as the temperature is raised in the range of 2 to 50 K (curves *1*), reaching zero above 50 K, the region in which NMR vanishes almost completely and PMR emerges. That being so, in contrast to the initial graphene sample (Fig. 9a, curve *1*) for which, as we noted above, the NMR exists almost throughout the studied temperature range, electrodeposition of cobalt particles (Fig. 9b, curve *1*) suppresses the NMR effect totally at temperatures as low as 130–140 K. Moreover, for the *MR* to flip the sign from negative to positive, the Co–*Gr*/SiO$_2$ sample requires weaker fields (Fig. 9b, curve *2*) than the initial graphene does (Fig. 9a, curve *2*). As can be seen, the most dramatic drop in $B_{\min}$ is observed when the temperature is raised in the range of 2–5 K, the range in which $R_\square(T)$ curves tend to saturation as the samples are cooled down (Fig. 4).

The presence of NMR in the region of relatively low magnetic fields is typically seen as a manifestation of contributions due to quantum corrections. It was reported [8] that commonly the following types of quantum corrections are considered in graphene with a high carrier mobility (e.g., in mechanically exfoliated graphene): weak localization as such and the one allowing for electron–electron coupling [6, 7, 33, 34]; the intervalley distance and break of chirality [34]; weak antilocalization [33, 34]; and more. According to the cited works, the listed contributions to the temperature dependences of graphene electrical resistance

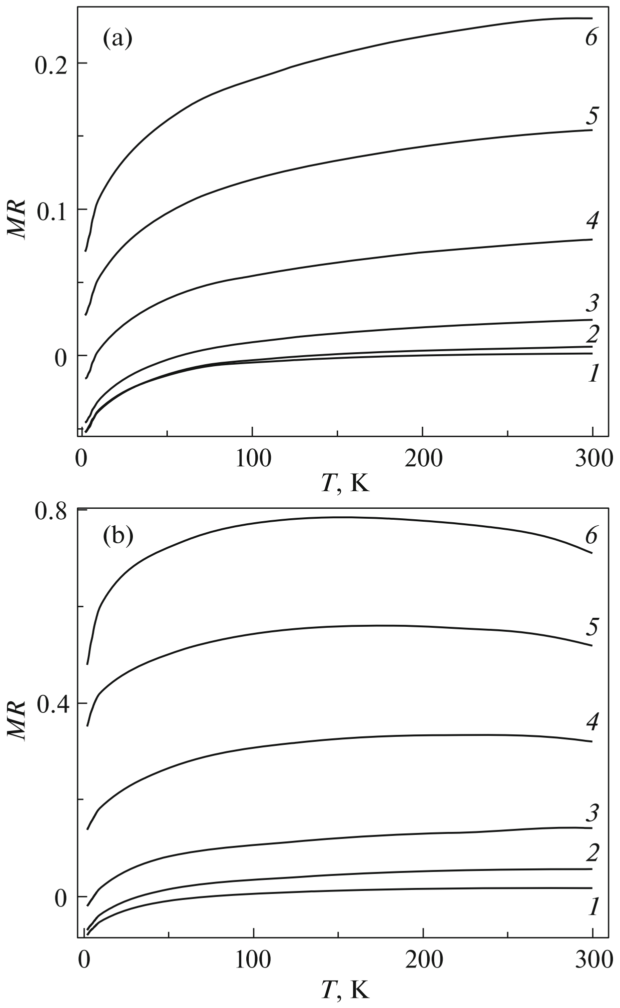

Fig. 8. Temperature dependences of relative magnetoresistance $MR(T)$ for (a) Gr/SiO_2 and (b) Co–Gr/SiO_2 samples in different magnetic fields B: (*1*) 0.5, (*2*) 1, (*3*) 2, (*4*) 4, (*5*) 6, and (*6*) 8 T.

can be both positive and negative. These are usually described by relationships of the type [35]

$$\Delta\sigma = \frac{e^2}{\pi h}\left(F\left(\frac{B}{B_\varphi}\right) - F\left(\frac{B}{B_\varphi + 2B_i}\right) - 2F\left(\frac{B}{B_\varphi + B_*}\right)\right), \quad (2)$$

where

$$F(x) = \ln(x) + \psi(0.5 + x^{-1}),$$

and the characteristic fields determine the phase incoherence of charge carriers for the corresponding process.

For the weak localization contribution, the time is given by the formula

$$\tau_\varphi = \frac{4eDB_\varphi}{\hbar}. \quad (3)$$

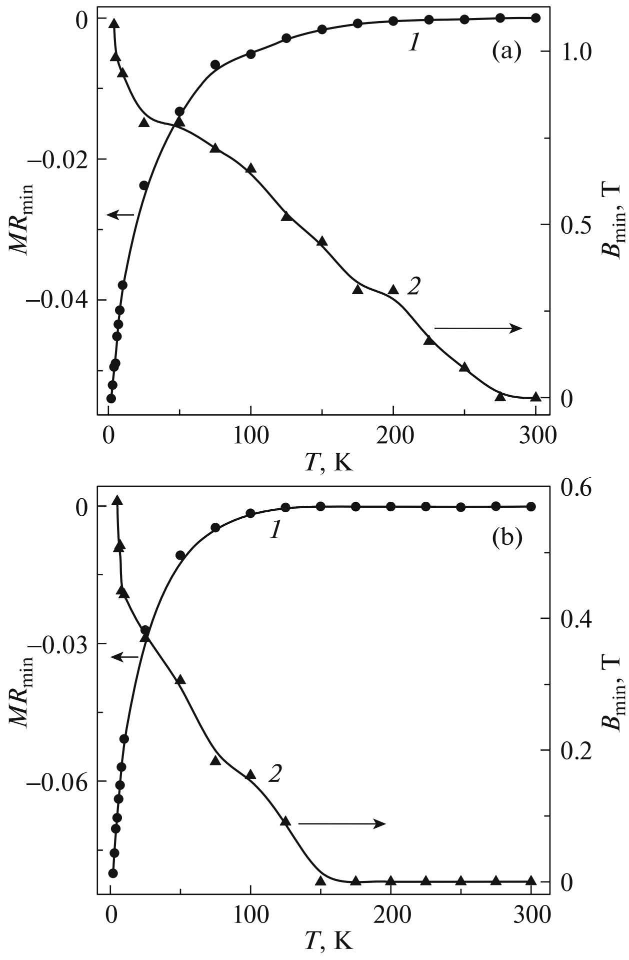

Fig. 9. Temperature dependences of (*1*) MR_{min} and (*2*) magnetic field B_{min} in minima of the $MR(B)$ curves shown in Figs. 7 and 8 for (a) Gr/SiO_2 and (b) Co–Gr/SiO_2 samples, respectively.

At the same time, within the quantum correction theory [36–38], the temperature dependences of phase incoherence time τ_φ of electron wave functions follow a power law:

$$\tau_\varphi(T) \sim T^{-p}, \quad (4)$$

where parameter p is determined by the mechanism underlying phase incoherence of electron wave functions, and the range predicted by the theory for this parameter is $1 < p < 2$ [27].

Equation (4) includes corrections due to weak localization (the first term), weak localization allowing for electron–electron coupling (the second term), and the effects of chirality and corrugations (the third term) [35, 39, 40]. With Eqs. (2) and (3), by performing data fitting, we can estimate the characteristic times of phase incoherence for the different contributions. The results of data fitting in the range of weak magnetic fields ($B < 1$, i.e., the range of existence of the NMR) are shown in Fig. 10. These corroborated

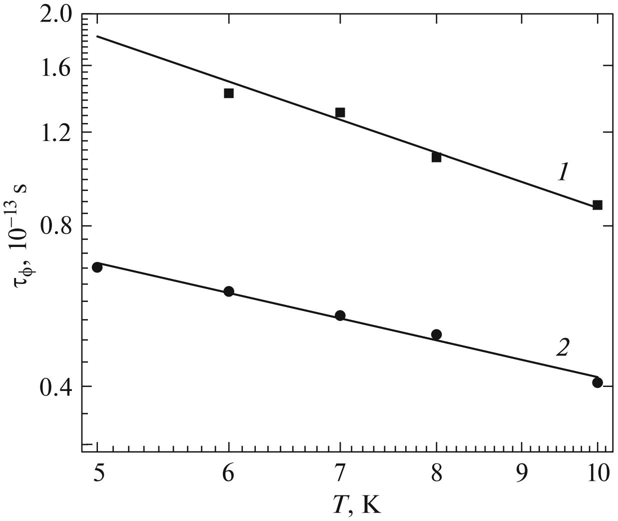

Fig. 10. Temperature dependences of phase incoherence times for the weak localization contribution to quantum corrections for (*1*) *Gr*/SiO_2 and (*2*) Co–*Gr*/SiO_2 samples.

the power law for the temperature dependence of phase incoherence time given by Eq. (6) and enabled us to determine the values for parameter p: 1.07 for the initial graphene (line *1*) and 0.71 for graphene with deposited cobalt particles (line *2*). Thus, the temperature dependence of $R_\square(T)$ in combination with magnetic field dependences $MP(B)$ suggest that the quantum corrections play a key role in the carrier transport at low temperatures in both the initial and cobalt nanoparticle-decorated graphene samples. The data fitting showed that in fields below 1 T and temperatures below 75 K the contribution of other terms entering Eq. (2) was no more than 0.1% of weak localization contribution. Their effect on low-temperature carrier transport may manifest in the PMR region, i.e., in stronger magnetic fields.

In summary, we can state that the decoration with cobalt particles has a considerable effect on both the temperature and field dependences of magnetization and sheet resistance of our samples; the effect is, however, different in different ranges of the temperature and magnetic flux density. Figure 11 shows temperature dependence of the difference of relative magnetoresistance effect—defined as $[MR_{\text{Co}-Gr}(T, 8\text{ T}) - MR_{Gr}(T, 8\text{ T})]$—for the *Gr*/$SiO_2$ and Co–*Gr*/SiO_2 samples in magnetic field $B = 8$ T, which enabled us to identify the contribution of cobalt particles to the magnetotransport in these samples. It can be seen that the curve has a maximum in a temperature range around 100 K, its position corresponding to the end of temperature range for the NMR in the Co–*Gr*/SiO_2 sample. As the temperature is raised above 250–275 K, the curve exhibits a sharp drop that coincides with a similar drop in sheet resistance $R_\square(T)$ (curves *2* in Fig. 4), which we previously related to the transition of CoO from the antiferromagnetic to paramagnetic state at a temperature above the Néel temperature.

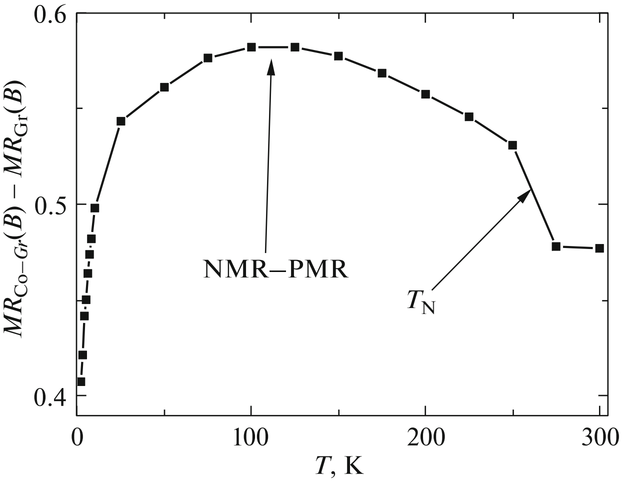

Fig. 11. Temperature dependences of the difference in relative magnetoresistance between *Gr*/SiO_2 and Co–*Gr*/SiO_2 samples, i.e., $[MR_{\text{Co}-Gr}(T, 8\text{ T}) - MR_{Gr}(T, 8\text{ T})]$, in a magnetic field $B = 8$ T. The critical temperature of NMR-to-PMR transition and the Néel temperature (T_N) for CoO are indicated with arrows.

We note that the decrease in the $[MR_{\text{Co}-Gr}(T, 8\text{ T}) - MR_{Gr}(T, 8\text{ T})]$ observed with increasing the temperature above 100 K can be considered as another argument in favor of the Lorentz mechanism contributing to the increase in PMR due to the influence of cobalt core, albeit we cannot fully eliminate the possibility of positive quantum corrections contributing to PMR [28].

4. CONCLUSIONS

We showed that electrochemical deposition onto CVD graphene in the pulse-reverse mode from an electrolyte containing $CoSO_4 \cdot 6H_2O$ produced Co–CoO particles (with size up to 500 nm) on the graphene surface consisting of polydisperse agglomerates with prolate shapes. For the Co–*Gr*/SiO_2 sample, the surface oxidation of cobalt particles is revealed in asymmetry in magnetization curves $M(H)$ and a dramatic decrease in sheet resistance $R(T)$ below the Neel temperature on their temperature dependences.

The deposition of Co–CoO particles was shown to increase the resistance of graphene samples due to a lower electron concentration. For the *Gr*/SiO_2 and Co–*Gr*/SiO_2 samples, we revealed the existence of a competition between the NMR and PMR contributions to the observed magnetoresistance effect and showed that the low-temperature carrier transport in the NMR region was due to quantum localization correction to the Drude model of conductivity, while the enhancement in PMR after depositing Co–CoO particles onto graphene may be attributed to the Lorentz mechanism operating within Co cores.

FUNDING

The work was supported by the State Committee on Science and Technology, Republic of Belarus (agreement no. F18PLShG-005), within the state research programs "Photonics and Opto- and Microelectronics" (assignment no. 3.3.01), and within a contract (no. 08626319/182161170-74) with the Joint Institute for Nuclear Research, Russia.

CONFLICT OF INTEREST

The authors declare that they have no conflicts of interest.

REFERENCES

1. I. S. Zhidkov, N. A. Skorikov, A. V. Korolev, A. I. Kukharenko, E. Z. Kurmaev, V. E. Fedorov, and S. O. Cholakh, Carbon **91**, 298 (2015).
2. P. U. Asshoff, J. L. Sambricio, A. P. Rooney, S. Slizovskiy, A. Mishchenko, A. M. Rakowski, E. W. Hill, A. K. Geim, S. J. Haigh, V. I. Fal'ko, I. J. Vera-Marun, and I. V. Grigorieva, 2D Mater. **4**, 031004 (2017).
3. M. Z. Iqbal, M. W. Iqbal, J. H. Lee, Y. S. Kim, S. Chun, and J. Eom, Nano Res. **6**, 373 (2013).
4. V. C. De Franco, G. M. B. Castro, J. Corredor, D. Mendes, and J. E. Schmidt, Carbon Lett. **21**, 16 (2017).
5. V. G. Bayev, J. A. Fedotova, J. V. Kasiuk, S. A. Vorobyova, A. A. Sohor, I. V. Komissarov, N. G. Kovalchuk, S. L. Prischepa, N. I. Kargin, M. Andrulevičius, J. Przewoznik, Cz. Kapusta, O. A. Ivashkevich, S. I. Tyutyunnikov, N. N. Kolobylina, and P. V. Guryeva, Appl. Surf. Sci. **440**, 1252 (2018).
6. B. L. Altshuler, A. G. Aronov, and D. E. Khmelnitsky, J. Phys. C **15**, 7367 (1982).
7. J. Jobst, D. Waldmann, I. V. Gornyi, A. D. Mirlin, and H. B. Weber, Phys. Rev. Lett. **108**, 106601 (2012).
8. S. V. Morozov, K. S. Novoselov, M. I. Katsnelson, F. Schedin, L. A. Ponomarenko, D. Jiang, and A. K. Geim, Phys. Rev. Lett. **97**, 016801 (2006).
9. B. I. Shklovskii and A. L. Efros, *Electronic properties of Doped Semiconductors*, Vol. 45 of *Springer Ser. Solid-State Sci.* (Springer, Heidelberg, 1984).
10. B. I. Shklovskii, Semiconductors **6**, 1964 (1973).
11. N. Mikoshiba, J. Phys. Chem. Solids **24**, 341 (1963).
12. S. A. Solin and L. R. Ram-Mohan, in *Handbook of Magnetism and Advanced Magnetic Materials* (Am. Cancer Soc., 2007), p. 19.
13. H. M. So, J. H. Mun, G. S. Bang, T. Y. Kim, B. J. Cho, and C. W. Ahn, Carbon Lett. **13**, 56 (2012).
14. A. C. Ferrari, J. C. Meyer, V. Scardaci, C. Casiraghi, M. Lazzeri, F. Mauri, S. Piscanec, D. Jiang, K. S. Novoselov, S. Roth, and A. K. Geim, Phys. Rev. Lett. **97**, 187401 (2006).
15. V. T. Nguyen, H. D. Le, V. C. Nguyen, T. T. T. Ngo, D. Q. Le, X. N. Nguyen, and N. M. Phan, Adv. Nat. Sci.: Nanosci. Nanotechnol. **4**, 035012 (2013).
16. X. Dong, P. Wang, W. Fang, C.-Y. Su, Y.-H. Chen, L.-J. Li, W. Huang, and P. Chen, Carbon **49**, 3672 (2011).
17. I. Shlimak, A. Haran, E. Zion, T. Havdala, Yu. Kaganovskii, A. V. Butenko, L. Wolfson, V. Richter, D. Naveh, A. Sharoni, E. Kogan, and M. Kaveh, Phys. Rev. B **91**, 045414 (2015).
18. H. Wang, Y. Wang, X. Cao, M. Feng, and G. Lan, J. Raman Spectrosc. **40**, 1791 (2009).
19. R. Saito, M. Hofmann, G. Dresselhaus, A. Jorio, and M. S. Dresselhaus, Adv. Phys. **60**, 413 (2011).
20. R. D. Gomez, M. C. Shih, R. M. H. New, R. F. W. Pease, and R. L. White, J. Appl. Phys. **80**, 342 (1996).
21. R. M. H. New, J. Vac. Sci. Technol. B **13**, 1089 (1995).
22. P. Ares, M. Jaafar, A. Gil, J. Gõmez-Herrero, and A. Asenjo, Small **11**, 4731 (2015).
23. J. Nogues, J. Sort, V. Langlais, V. Skumryev, S. Suriñach, J. S. Muñoz, and M. D. Baró, Phys. Rep. **422**, 65 (2005).
24. R. López Antón, J. A. González, J. P. Andrés, J. Canales-Vázquez, J. A. de Toro, and J. M. Riveiro, Nanotechnology **25**, 105702 (2014).
25. S. Sako, K. Ohshima, M. Sakai, and S. Bandow, Surf. Rev. Lett. **3**, 109 (1996).
26. K. Takehana, Y. Imanaka, E. Watanabe, H. Oosato, D. Tsuya, Y. Kim, and Ki-Seok An, Curr. Appl. Phys. **17**, 474 (2017).
27. V. M. Pudalov, Proc. Int. Sch. Phys. "Enrico Fermi" **157**, 335 (2004).
28. E. Zion, A. Haran, A. Butenko, L. Wolfson, Y. Kaganovskii, T. Havdala, A. Sharoni, D. Naveh, V. Richter, M. Kaveh, E. Kogan, and I. Shlimak, Graphene **4**, 45 (2015).
29. T. A. Polyanskaya and Yu. V. Shmartsev, Sov. Phys. Semicond. **23**, 1 (1989).
30. V. K. Tewary and B. Yang, Phys. Rev. B **79**, 125416 (2009).
31. F. V. Tikhonenko, D. W. Horsell, R. V. Gorbachev, and A. K. Savchenko, Phys. Rev. Lett. **100**, 056802 (2008).
32. N. F. Mott and E. A. Davis, *Electronic Processes in Non-Crystalline Materials*, 2nd ed. (Oxford Univ. Press, Oxford, 1979).
33. R. V. Gorbachev, F. V. Tikhonenko, A. S. Mayorov, D. W. Horsell, and A. Savchenko, Phys. Rev. Lett. **98**, 176805 (2007).
34. K. Kechedzhi, E. Mccann, V. I. Fal'ko, H. Suzuura, T. Ando, and B. L. Altshuler, Eur. Phys. J. Spec. Top. **148**, 39 (2007).
35. E. McCann, K. Kechedzhi, V. I. Fal'ko, H. Suzuura, T. Ando, and B. L. Altshuler, Phys. Rev. Lett. **97**, 146805 (2006).
36. B. L. Altshuler and A. G. Aronov, Mod. Probl. Condens. Matter Sci. **10**, 1 (1985).
37. R. Oppermann, M. J. Schmidt, and D. Sherrington, Phys. Rev. Lett. **98**, 127201 (2007).
38. A. V. Germanenko, G. M. Minkov, and O. E. Rut, Phys. Rev. B **64**, 165404 (2001).
39. C. W. J. Beenakker and H. V. Houten, Solid State Phys. **44**, 1 (1991).
40. B. L. Altshuler, D. Khmel'nitzkii, A. I. Larkin, and P. A. Lee, Phys. Rev. B **22**, 5142 (1980).

Translated by A. Kukharuk